IMAGING MULTIPOLE SELF-POTENTIAL SOURCES BY 3D PROBABILITY TOMOGRAPHY

R. Alaia and D. Patella

Department of Physical Sciences
University Federico II
Naples, Italy

P. Mauriello

Department of Science and Technology for Environment and Territory
University of Molise
Campobasso, Italy

Abstract—We present the theoretical development of the 3D multipole probability tomography applied to the electric Self-Potential (SP) method of geophysical exploration. We assume that an SP dataset can be thought of as the response of an aggregation of poles, dipoles, quadrupoles and octopoles. These physical sources are used to reconstruct, without a priori assumptions, the most probable position and shape of the true SP buried sources, by determining the location of their centres and critical points of their boundaries, as corners, wedges and vertices. At first, a few synthetic cases with cubic bodies are examined in order to determine the resolution power of the new technique. Then, an experimental SP dataset collected in the Mt. Somma-Vesuvius volcanic district (Naples, Italy) is elaborated in order to define location and shape of the sources of two SP anomalies of opposite sign detected in the northwestern sector of the surveyed area. The modelled sources are interpreted as the polarization state induced by an intense hydrothermal convective flow mechanism within the volcanic apparatus, from the free surface down to about 3 km of depth b.s.l.

Corresponding author: D. Patella (patella@na.infn.it).

1. INTRODUCTION

Probability tomography is an algorithm used to image the most probable localization and shape of the buried sources of the anomalies appearing in a geophysical dataset. This approach was originally formulated for the electric self-potential (SP) method [1, 2] and successively applied to other prospecting methods [3–9]. In all of these developments, the sources were assimilated to aggregates of polar and/or dipolar point sources.

An extension of the original theory has recently been proposed for the geoelectric method, by assuming a dataset to be the conjoint response of poles, dipoles and quadrupoles. In practical applications, these simple sources have been used to find the most probable location of the centres and some peculiar points of the boundaries of the real bodies [10, 11].

The aim of this paper is to adapt the new formulation to the specific properties of the SP electrical field, by also including the response due to octopoles. This extended multipole analysis may allow a much denser set of critical points to be imaged for a better delineation of the full shape of the most probable SP sources, within the limits of the dataset information content. A few tests on simple cubic models and the analysis of a field SP survey in the active volcanic area of Mt. Somma-Vesuvius (Naples, Italy) will be discussed, in order to evaluate both feasibility and reliability of the new approach to the SP source modelling.

2. OUTLINE OF THE SP METHOD

2.1. The SP Phenomenology and Measuring Technique

The SP measurements refer to that part of the natural electrical field which is stationary in time, or slowly varying in relation to the time span required for the execution of a survey, and whose current source system is generated and sustained by phenomena occurring underground within geological structures. The most important source mechanism in rocks, which has been proposed to explain SP field data both in exploration geophysics and in tectonophysics, is the so called electrokinetic effect related to the movement of fluids in porous systems in presence of an electrical double layer at the fluid-rock matrix interface. Basically, the electrokinetic effect is included within the constitutive relationships that formalise Onsager's coupled flow theory [12]. From the physical point of view, the common aspect of the many source models is that an electrical charge polarization is developed, which is assumed to be responsible for the electrical

current circulation in conductive rocks. It follows that the detected SP anomalies are simply the surface evidence of a more or less steady state of electric polarization.

SP data are collected in field surveys as potential drops, ΔU, across a passive dipole, normally consisting of a pair of liquid junction copper-copper sulphate porous pots as grounded electrodes. If the dipole length is sufficiently small relative to the expected anomaly wavelengths, the ratio SP drop to dipole length gives an estimate of the component of the natural electrical field along the dipole axis on the measurement surface. The sequence of progressive readings of this ratio along a survey line is currently known as the gradient technique and is the most commonly used procedure in difficult areas. Furthermore, a standard polarity cable-connecting convention, with reversal of leading and trailing electrodes between successive measurements, known as the leapfrog profiling technique, permits measurement of SP data which is virtually free of electrode polarization error. Finally, the use of loops or two-way profiles helps to eliminate virtually any spurious effects of SP drift, by distributing the tie-in closure error among all the readings around the closed circuit [13].

2.2. Structure of the SP Electric Field Surface Components

Let us consider a reference system with a horizontal (x, y)-plane placed at sea level and the z-axis positive downwards, and a 2D datum domain S as in Figure 1. The S-domain is generally a non-flat ground survey area described by a topographic height function $z(x, y)$. We indicate with $\mathbf{E}_S(\mathbf{r})$ the SP electrical field vector at a set of datum points $\mathbf{r} \equiv [x, y, z(x, y)]$, with $\mathbf{r} \in S$.

In areas with rough topography and inaccessible sites the current practice in collecting SP data consists of a continuous displacement of the measuring dipole along a generally irregular network of closed circuits and/or two-way interconnected branched lines. In order to provide a uniform and dense distribution of $\mathbf{E}_S(\mathbf{r})$ data, a pre-processing is required according to the following three steps [2].

The first step consists in assigning a zero potential value to an arbitrary reference point in the area, where an electrode had been placed, and in recovering from the original sequence of SP drops, a new sequence of SP values by simple algebraic summation. The second step consists in contouring the new set of potential data, in order to draw a SP anomaly map covering the entire survey area, as sketched in Figure 1. The third step consists in selecting a double set of curvilinear φ- and ψ-profiles following the height variations of the ground, such that their projections onto the horizontal (x, y)-plane are parallel to the x-axis and y-axis and equally spaced from each other
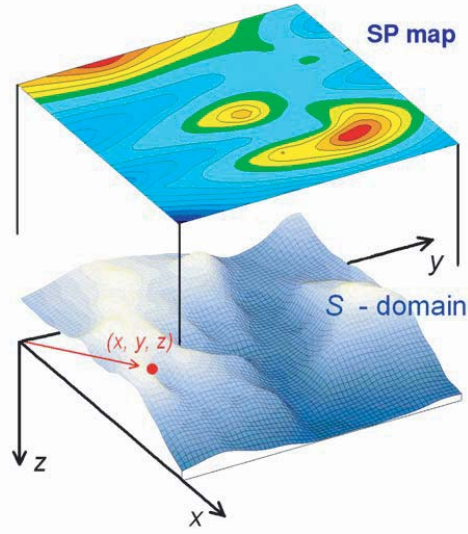
Figure 1. The datum domain (S-domain) generating the SP map on top. The (x, y)-plane is placed at sea level and the z-axis points into the earth.

by the spacings Δy and Δx, respectively. Along any φ-profile or ψ-profile, the sampling interval projection onto the (x, y)-plane, equal to Δx or Δy, respectively, is assumed constant and, for the sake of easier calculations, such that $\Delta x = \Delta y = \Delta \tau$, where $\Delta \tau$ is taken from now on as the unique distance discretization element. Using a regular square grid on the (x, y)-plane, at each cross point of every pair of perpendicular x-line and y-line, a pair of values of the electrical field components, $E_\varphi(\mathbf{r})$ and $E_\psi(\mathbf{r})$, is assigned. These are estimated by interpolation from the SP map across dipoles of length $\Delta \varphi$ and $\Delta \psi$, respectively and attributed to the midpoint of the projected dipoles, both of length $\Delta \tau$. By indicating with ΔU_φ and ΔU_ψ the potential difference across $\Delta \varphi$ and $\Delta \psi$, respectively, we readily obtain the estimates of $E_\varphi(\mathbf{r})$ and $E_\psi(\mathbf{r})$ as

$$E_\varphi(\mathbf{r}) = -\frac{\Delta U_\varphi(\mathbf{r})}{\Delta \varphi} = -\frac{\Delta U_\varphi(\mathbf{r})}{\Delta \tau \left[1 + (\Delta z/\Delta \tau)^2\right]^{1/2}}, \tag{1a}$$

$$E_\psi(\mathbf{r}) = -\frac{\Delta U_\psi(\mathbf{r})}{\Delta \psi} = -\frac{\Delta U_\psi(\mathbf{r})}{\Delta \tau \left[1 + (\Delta z/\Delta \tau)^2\right]^{1/2}}. \tag{1b}$$

3. THE SP PROBABILITY TOMOGRAPHY THEORY

3.1. The SP Electric Field Vector Function and Its Power

We assume that $\mathbf{E}_S(\mathbf{r})$ can be discretised as

$$
\mathbf{E}_S(\mathbf{r}) = \sum_{m=1}^{M} (\mathbf{p}_m \cdot \mathbf{P}_m)\, \mathbf{s}(\mathbf{r}, \mathbf{r}_m) + \sum_{n=1}^{N} (\mathbf{d}_n^u \cdot \mathbf{L}_n^u)\, \mathbf{s}(\mathbf{r}, \mathbf{r}_n)
$$
$$
+ \sum_{g=1}^{G} \left(\mathbf{q}_g^{uv} \cdot \mathbf{S}_g^{uv}\right) \mathbf{s}(\mathbf{r}, \mathbf{r}_g) + \sum_{h=1}^{H} (\mathbf{o}_h^{uvw} \cdot \mathbf{C}_h^{uvw})\, \mathbf{s}(\mathbf{r}, \mathbf{r}_h), \quad (2)
$$

i.e., as a sum of effects due to:

- a set of M poles, the mth element of which is located at $\mathbf{r}_m \equiv (x_m, y_m, z_m)$ and has strength $\mathbf{p}_m \cdot \mathbf{P}_m$, where $\mathbf{p}_m$ and $\mathbf{P}_m$ are the pole moment and a point operator 0th-order tensor, respectively;
- a set of N dipoles, whose nth element is located at $\mathbf{r}_n \equiv (x_n, y_n, z_n)$ with strength $(\mathbf{d}_n^u \cdot \mathbf{L}_n^u)$ $(u = x, y, z)$, where $\mathbf{d}_n^u$ and $\mathbf{L}_n^u$ are the dipole moment and a line operator 1st-order tensor, respectively;
- a set of G quadrupoles, whose gth element is located at $\mathbf{r}_g \equiv (x_g, y_g, z_g)$ with strength $(\mathbf{q}_g^{uv} \cdot \mathbf{S}_g^{uv})$ $(u, v = x, y, z)$, where $\mathbf{q}_g^{uv}$ and $\mathbf{S}_g^{uv}$, respectively, are the quadrupole moment and a square operator 2nd-order tensor;
- a set of H octopoles, whose hth element is located at $\mathbf{r}_h \equiv (x_h, y_h, z_h)$ and has strength $(\mathbf{o}_h^{uvw} \cdot \mathbf{C}_h^{uvw})$ $(u, v, w = x, y, z)$, where $\mathbf{o}_h^{uvw}$ and $\mathbf{C}_h^{uvw}$ are the octopole moment and a cube operator 3rd-order tensor, respectively.

The dot in the definition of the source strength tensors indicates inner product. The operator tensors $\mathbf{P}$, $\mathbf{L}^u$, $\mathbf{S}^{uv}$ and $\mathbf{C}^{uvw}$ $(u, v, w = x, y, z)$ are made geometrically explicit in Figure 2.

The effect of the M, N, G and H source elements at a point $\mathbf{r} \in S$ is determined by the vector kernel $\mathbf{s}(\mathbf{r}, \mathbf{r}_i)$ $(i = m, n, g, h)$, which represents the electrical field vector due to a point positive charge of unitary strength. The components $s_\varphi(\mathbf{r}, \mathbf{r}_i)$ and $s_\psi(\mathbf{r}, \mathbf{r}_i)$ of $\mathbf{s}(\mathbf{r}, \mathbf{r}_i)$ over the S-domain are explicitly given as

$$
s_\varphi(\mathbf{r}, \mathbf{r}_i) = \frac{(x - x_i) + (z - z_i)\, z_x'}{\left[(x - x_i)^2 + (y - y_i)^2 + (z - z_i)^2\right]^{3/2}} x_\varphi', \qquad (3a)
$$

$$
s_\psi(\mathbf{r}, \mathbf{r}_i) = \frac{(y - y_i) + (z - z_i) z_y'}{\left[(x - x_i)^2 + (y - y_i)^2 + (z - z_i)^2\right]^{3/2}} y_\psi', \qquad (3b)
$$
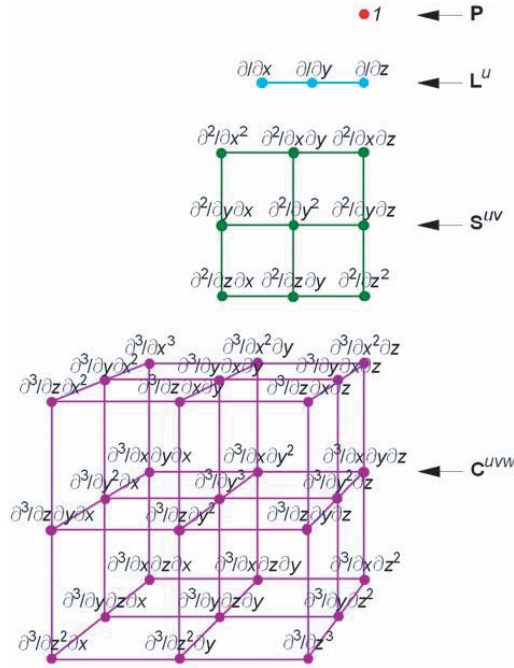
Figure 2. Explicit representation of the symbolic tensor operators appearing in the definition of the strengths of the pole, dipole, quadrupole and octopole source elements defined in Eq. (2).

where it is $z'_x = \partial z/\partial x$, $z'_y = \partial z/\partial y$, $x'_\varphi = \mathrm{d}x/\mathrm{d}\varphi$ and $y'_\psi = \mathrm{d}y/\mathrm{d}\psi$.

We define the information power Λ, associated with $\mathbf{E}_S(\mathbf{r})$, over the surface S as

$$\Lambda = \int_S \mathbf{E}_S(\mathbf{r}) \cdot \mathbf{E}_S(\mathbf{r}) dS, \tag{4a}$$

which, using Eq. (2), is expanded as

$$\Lambda = \sum_{m=1}^{M} p_m \int_S \mathbf{E}_S(\mathbf{r}) \cdot \mathbf{s}(\mathbf{r}, \mathbf{r}_m) dS + \sum_{n=1}^{N} \sum_{u=x,y,z} d_n^u \int_S \mathbf{E}_S(\mathbf{r}) \cdot \frac{\partial \mathbf{s}(\mathbf{r}, \mathbf{r}_n)}{\partial u_n} dS$$

$$+ \sum_{g=1}^{G} \sum_{u=x,y,z} \sum_{v=x,y,z} q_g^{uv} \int_S \mathbf{E}_S(\mathbf{r}) \cdot \frac{\partial^2 \mathbf{s}(\mathbf{r}, \mathbf{r}_g)}{\partial u_g \partial v_g} dS$$

$$+ \sum_{h=1}^{H} \sum_{u=x,y,z} \sum_{v=x,y,z} \sum_{w=x,y,z} o_h^{uvw} \int_S \mathbf{E}_S(\mathbf{r}) \cdot \frac{\partial^3 \mathbf{s}(\mathbf{r}, \mathbf{r}_h)}{\partial u_h \partial v_h \partial w_h} dS \tag{4b}$$

3.2. The SP Source Pole Occurrence Probability

We consider a generic mth integral of the first sum in Eq. (4b) and apply Schwarz inequality, thus obtaining

$$\left[\int_S \mathbf{E}_S(\mathbf{r}) \cdot \mathbf{s}(\mathbf{r}, \mathbf{r}_m) \mathrm{d}S\right]^2 \le \int_S E_S^2(\mathbf{r}) \mathrm{d}S \int_S s^2(\mathbf{r}, \mathbf{r}_m) dS. \qquad (5)$$

Inequality (5) is used to define a source pole occurrence probability (SPOP) function as [2]

$$\eta_m^{(p)} = C_m^{(p)} \int_S \mathbf{E}_S(\mathbf{r}) \cdot \mathbf{s}(\mathbf{r}, \mathbf{r}_m) dS, \qquad (6a)$$

where

$$C_m^{(p)} = \left[\int_S E_S^2(\mathbf{r}) dS \int_S s^2(\mathbf{r}, \mathbf{r}_m) dS\right]^{-1/2} \qquad (6b)$$

and $\mathbf{s}(\mathbf{r}, \mathbf{r}_m)$ has the role of source pole scanner. The explicit formulae of the components $s_\varphi(\mathbf{r}, \mathbf{r}_m)$ and $s_\psi(\mathbf{r}, \mathbf{r}_m)$ of $\mathbf{s}(\mathbf{r}, \mathbf{r}_m)$ over the S-domain are those reported in Eq. (3a) and Eq. (3b), respectively, putting $i = m$.

The 3D SPOP function, which satisfies the condition $-1 \le \eta_m^{(p)} \le 1$, is given as a measure of the probability of a source pole of strength p_m placed at $\mathbf{r}_m$, being responsible for the observed $\mathbf{E}_S(\mathbf{r})$ field. Each $\eta_m^{(p)}$ indicates the occurrence probability of a positive, null or negative electrical charge in each location.

For computational purposes, we proceed as follows. We assume that the projection of S onto the (x, y)-plane can be fitted to a rectangle R of sides $2X$ and $2Y$ along the x-axis and y-axis, respectively. Using the topography surface regularization factor $g(z)$ given by [2]

$$g(z) = \left[1 + (\partial z/dx)^2 + (\partial z/dy)^2\right]^{1/2} \qquad (7)$$

Eq. (6a) is definitely written as

$$\eta_m^{(p)} = C_m^{(p)} \int_{-X}^{+X} \int_{-Y}^{+Y} \mathbf{E}_S(\mathbf{r}) \cdot \mathbf{s}(\mathbf{r}, \mathbf{r}_m) g(z) dx dy, \qquad (8a)$$

with

$$C_m^{(p)} = \Big[\int\limits_{-X}^{+X} \int\limits_{-Y}^{+Y} E_S^2(\mathbf{r})g(z)dxdy \cdot \int\limits_{-X}^{+X} \int\limits_{-Y}^{+Y} s^2(\mathbf{r}, \mathbf{r}_m)g(z)dxdy \Big]^{-1/2}. \quad (8b)$$

3.3. The SP Source Dipole Occurrence Probability

We take a generic nth integral of the second sum in Eq. (4b) and apply, as previously, Schwarz's inequality to each u-component. We can thus define a source dipole occurrence probability (SDOP) function as [9]

$$\eta_{n,u}^{(d)} = C_{n,u}^{(d)} \int\limits_{-X}^{+X} \int\limits_{-Y}^{+Y} \mathbf{E}_S(\mathbf{r}) \cdot \frac{\partial \mathbf{s}(\mathbf{r}, \mathbf{r}_n)}{\partial u_n} g(z)dxdy, \quad (u = x, y, z) \quad (9a)$$

with

$$C_{n,u}^{(d)} = \Big[\int\limits_{-X}^{+X} \int\limits_{-Y}^{+Y} E_S^2(\mathbf{r})g(z)dxdy \cdot \int\limits_{-X}^{+X} \int\limits_{-Y}^{+Y} \Big| \frac{\partial \mathbf{s}(\mathbf{r}, \mathbf{r}_n)}{\partial u_n} \Big|^2 g(z)dxdy \Big]^{-1/2}. \quad (9b)$$

Also $\eta_{n,u}^{(d)}$ falls in the range $[-1, 1]$. Thus, at each $\mathbf{r}_n$, 3 values of $\eta_{n,u}^{(d)}$ can be computed. They are interpreted as a measure of the probability of a single source dipole located at $\mathbf{r}_n$, being responsible of the whole $\mathbf{E}_S(\mathbf{r})$ field. Each first derivative of $\mathbf{s}(\mathbf{r}, \mathbf{r}_n)$ has the role of source dipole scanner. The first derivatives of the components $s_\varphi(\mathbf{r}, \mathbf{r}_n)$ and $s_\psi(\mathbf{r}, \mathbf{r}_n)$ of $\mathbf{s}(\mathbf{r}, \mathbf{r}_n)$ over the S-domain are derived, respectively, from Eq. (3a) and Eq. (3b) as

$$\frac{\partial s_\varphi(\mathbf{r}, \mathbf{r}_n)}{\partial x_n} = \frac{3(x - x_n)A_{1,n}(x, z) - |\mathbf{r} - \mathbf{r}_n|^2}{|\mathbf{r} - \mathbf{r}_n|^5} x'_\varphi, \quad (10a)$$

$$\frac{\partial s_\varphi(\mathbf{r}, \mathbf{r}_n)}{\partial y_n} = \frac{3(y - y_n)A_{1,n}(x, z)}{|\mathbf{r} - \mathbf{r}_n|^5} x'_\varphi, \quad (10b)$$

$$\frac{\partial s_\varphi(\mathbf{r}, \mathbf{r}_n)}{\partial z_n} = \frac{3(z - z_n)A_{1,n}(x, z) - |\mathbf{r} - \mathbf{r}_n|^2 z'_x}{|\mathbf{r} - \mathbf{r}_n|^5} x'_\varphi, \quad (10c)$$

$$\frac{\partial s_\psi(\mathbf{r}, \mathbf{r}_n)}{\partial x_n} = \frac{3(x - x_n)B_{1,n}(y, z)}{|\mathbf{r} - \mathbf{r}_n|^5} y'_\psi, \quad (10d)$$

$$\frac{\partial s_\psi(\mathbf{r}, \mathbf{r}_n)}{\partial y_n} = \frac{3(y - y_n)B_{1,n}(y, z) - |\mathbf{r} - \mathbf{r}_n|^2}{|\mathbf{r} - \mathbf{r}_n|^5} y'_\psi, \quad (10e)$$

$$\frac{\partial s_\psi(\mathbf{r}, \mathbf{r}_n)}{\partial z_n} = \frac{3(z - z_n)B_{1,n}(y, z) - |\mathbf{r} - \mathbf{r}_n|^2 z_y'}{|\mathbf{r} - \mathbf{r}_n|^5} y_\psi', \qquad (10f)$$

with $A_{1,n}(x, z) = (x - x_n) + (z - z_n)z_x'$, $B_{1,n}(y, z) = (y - y_n) + (z - z_n)z_y'$.

3.4. The SP Source Quadrupole Occurrence Probability

Accordingly, we consider now a generic gth integral of the third sum in Eq. (4b) and apply Schwarz's inequality to each uv-element ($u, v = x, y, z$), which allows a source quadrupole occurrence probability (SQOP) function to be defined as [10]

$$\eta_{g,uv}^{(q)} = C_{g,uv}^{(q)} \int\limits_{-X}^{+X} \int\limits_{-Y}^{+Y} \mathbf{E}_S(\mathbf{r}) \cdot \frac{\partial^2 \mathbf{s}(\mathbf{r}, \mathbf{r}_g)}{\partial u_g \partial v_g} g(z) dx dy, \qquad (11a)$$

with

$$C_{g,uv}^{(q)} = \Bigg[\int\limits_{-X}^{+X} \int\limits_{-Y}^{+Y} E_S^2(\mathbf{r}) g(z) dx dy \cdot \int\limits_{-X}^{+X} \int\limits_{-Y}^{+Y} \Bigg| \frac{\partial^2 \mathbf{s}(\mathbf{r}, \mathbf{r}_g)}{\partial u_g \partial v_g} \Bigg|^2 g(z) dx dy \Bigg]^{-1/2}. \quad (11b)$$

As before, the 3D SQOP function also falls in the range $[-1, 1]$. Thus, at each point $\mathbf{r}_g$, 9 values of $\eta_{g,uv}^{(q)}$ are taken as a measure of the probability for a quadrupole source located at $\mathbf{r}_g$, to be responsible of the $\mathbf{E}_S(\mathbf{r})$ dataset. Since $\mathbf{S}_g^{uv}$ is a symmetric square tensor, it follows that $\eta_{g,uv}^{(q)} = \eta_{g,vu}^{(q)}$. Therefore, at each $\mathbf{r}_g$, the 3 diagonal plus the 3 right-up or left-down off-diagonal terms of $\eta_{g,uv}^{(q)}$ are sufficient. However, as we are interested in finding the position of the corners of a source body, we will finally consider only the 3 off-diagonal terms ($u \neq v$) [10].

Each second derivative of $\mathbf{s}(\mathbf{r}, \mathbf{r}_g)$ has the role of source quadrupole scanner. The useful second derivatives of the components $s_\varphi(\mathbf{r}, \mathbf{r}_g)$ and $s_\psi(\mathbf{r}, \mathbf{r}_g)$ of $\mathbf{s}(\mathbf{r}, \mathbf{r}_g)$ over the S-domain are derived, respectively, from Eq. (3a) and Eq. (3b) as

$$\frac{\partial^2 s_\varphi(\mathbf{r}, \mathbf{r}_g)}{\partial x_g \partial y_g} = \frac{3(y - y_g)\Big[5(x - x_g)A_{1,g}(x, z) - |\mathbf{r} - \mathbf{r}_g|^2\Big]}{|\mathbf{r} - \mathbf{r}_g|^7} x_\varphi', \qquad (12a)$$

$$\frac{\partial^2 s_\varphi(\mathbf{r}, \mathbf{r}_g)}{\partial x_g \partial z_g} = \frac{15(x - x_g)(z - z_g)A_{1,g}(x, z) - 3A_{2,g}(x, z)|\mathbf{r} - \mathbf{r}_g|^2}{|\mathbf{r} - \mathbf{r}_g|^7} x_\varphi', \quad (12b)$$

$$\frac{\partial^2 s_\varphi(\mathbf{r}, \mathbf{r}_g)}{\partial y_g \partial z_g} = \frac{3(y - y_g)\Big[5(z - z_g)A_{1,g}(x, z) - |\mathbf{r} - \mathbf{r}_g|^2 z_x'\Big]}{|\mathbf{r} - \mathbf{r}_g|^7} x_\varphi', \qquad (12c)$$

$$\frac{\partial^2 s_\psi(\mathbf{r},\mathbf{r}_g)}{\partial x_g \partial y_g} = \frac{3(x-x_g)\left[5(y-y_g)B_{1,g}(y,z) - |\mathbf{r}-\mathbf{r}_g|^2\right]}{|\mathbf{r}-\mathbf{r}_g|^7} y'_\psi, \qquad (12\mathrm{d})$$

$$\frac{\partial^2 s_\psi(\mathbf{r},\mathbf{r}_g)}{\partial x_g \partial z_g} = \frac{3(x-x_g)\left[5(z-z_g)B_{1,g}(y,z) - |\mathbf{r}-\mathbf{r}_g|^2\, z'_y\right]}{|\mathbf{r}-\mathbf{r}_g|^7} y'_\psi, \quad (12\mathrm{e})$$

$$\frac{\partial^2 s_\psi(\mathbf{r},\mathbf{r}_g)}{\partial y_g \partial z_g} = \frac{15(y-y_g)(z-z_g)B_{1,g}(y,z) - 3B_{2,g}(y,z)|\mathbf{r}-\mathbf{r}_g|^2}{|\mathbf{r}-\mathbf{r}_g|^7} y'_\psi \quad (12\mathrm{f})$$

with $A_{1,g}(x,z) = (x-x_g)+(z-z_g)z'_x$, $A_{2,g}(x,z) = (z-z_g)+(x-x_g)z'_x$, $B_{1,g}(x,z) = (y-y_g)+(z-z_g)z'_y$ and $B_{2,g}(x,z) = (z-z_g)+(y-y_g)z'_y$.

3.5. The SP Source Octopole Occurrence Probability

Finally, we consider a generic hth integral of the fourth sum in Eq. (4b) and apply again Schwarz's inequality to each uvw-term $(u,v,w = x,y,z)$, allowing a source octopole occurrence probability (SOOP) function to be defined as

$$\eta^{(o)}_{h,\,uvw} = C^{(o)}_{h,\,uvw} \int\limits_{-X}^{+X}\int\limits_{-Y}^{+Y} \mathbf{E}_S(\mathbf{r}) \cdot \frac{\partial^3 \mathbf{s}(\mathbf{r},\mathbf{r}_h)}{\partial u_h \partial v_h \partial w_h} g(z) dx dy, \qquad (13\mathrm{a})$$

with

$$C^{(o)}_{h,uvw} = \left[\int\limits_{-X}^{+X}\int\limits_{-Y}^{+Y} E_S^2(\mathbf{r})g(z)dxdy \cdot \int\limits_{-X}^{+X}\int\limits_{-Y}^{+Y} \left|\frac{\partial^3 \mathbf{s}(\mathbf{r},\mathbf{r}_h)}{\partial u_h \partial v_h \partial w_h}\right|^2 g(z)dxdy\right]^{-1/2}. \quad (13\mathrm{b})$$

As noted above, the 3D SOOP function falls in the range $[-1,1]$. At each $\mathbf{r}_h$, 27 values may now be calculated, each interpreted as a probability measure of a single octopole source located at $\mathbf{r}_h$, being responsible of the whole $\mathbf{E}_S(\mathbf{r})$ dataset. However, as we are interested in finding only the position of the vertices of a source body, we will limit our analysis only to the SOOP function with $u \neq v \neq w$.

Each third derivative of $\mathbf{s}(\mathbf{r},\mathbf{r}_h)$ takes the role of source octopole scanner. The useful third derivatives of the components $s_\varphi(\mathbf{r},\mathbf{r}_h)$ and $s_\psi(\mathbf{r},\mathbf{r}_h)$ of $\mathbf{s}(\mathbf{r},\mathbf{r}_h)$ over the S-domain are derived, respectively, from Eq. (3a) and Eq. (3b) as

$$\frac{\partial^3 s_\varphi(\mathbf{r},\mathbf{r}_h)}{\partial x_h \partial y_h \partial z_h} = \frac{15(y-y_h)\left[7(x-x_h)(z-z_h)A_{1,h}(x,z)A_{2,h}(x,z)\,|\mathbf{r}-\mathbf{r}_h|^2\right]}{|\mathbf{r}-\mathbf{r}_h|^9} x'_\varphi, \quad (14\mathrm{a})$$

$$\frac{\partial^3 s_\psi(\underline{\mathrm{fr}},\mathbf{r}_h)}{\partial x_h \partial y_h \partial z_h} = \frac{15(x-x_h)\left[7(y-y_h)(z-z_h)B_{1,h}(y,z) - B_{2,h}(y,z)\,|\mathbf{r}-\mathbf{r}_h|^2\right]}{|\mathbf{r}-\mathbf{r}_h|^9} y'_\psi \quad (14\mathrm{b})$$

with $A_{1,h}(x,z) = (x-x_h)+(z-z_h)z'_x$, $A_{2,h}(x,z) = (z-z_h)+(x-x_h)z'_x$, $B_{1,h}(x,z) = (y-y_h)+(z-z_h)z'_y$ and $B_{2,h}(x,z) = (z-z_h)+(y-y_h)z'_y$.

4. SYNTHETIC EXAMPLES

We show some synthetic examples, in order to outline the main aspects of the multipole generalisation of the SP probability tomography.

4.1. The Coaxial Cube Model

At first, we consider a coaxial cube model with sides $6\,\mathrm{m}$ long parallel to the coordinate axes and centre at $x = 0$, $y = 0$, $z = 6\,\mathrm{m}$. A positive charge of $0.5\,\mathrm{C}$ is assumed uniformly distributed on the surface of the cube with a charge surface density $\Delta\sigma \cong 2.315 \cdot 10^{-3}\,\mathrm{C/m^2}$. The SP data have been computed at the nodes of a Cartesian grid where the elements are unit squares, using a $1\,\mathrm{m}$ step from $-18\,\mathrm{m}$ to $18\,\mathrm{m}$ along both x-axis and y-axis. Figure 3 shows the synthetic SP map on the
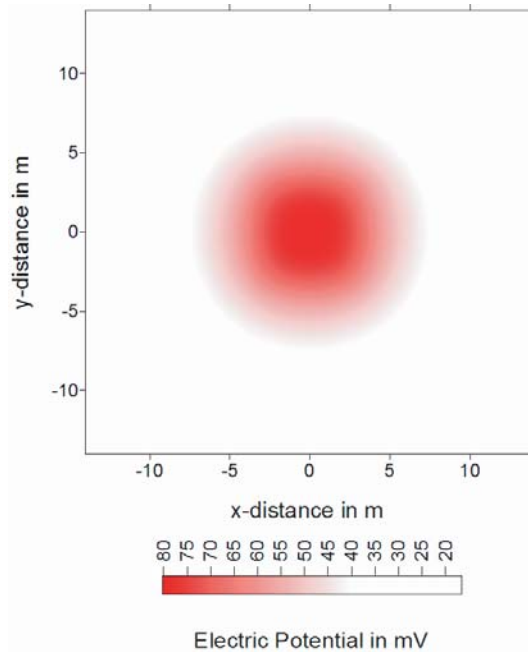
Figure 3. The SP map for the cube model with a positive charge surface density $\Delta\sigma \cong 2.315 \cdot 10^{-3}\,\mathrm{C/m^2}$, sides $6\,\mathrm{m}$ long and centre at $x = 0$, $y = 0$ and $z = 6\,\mathrm{m}$.
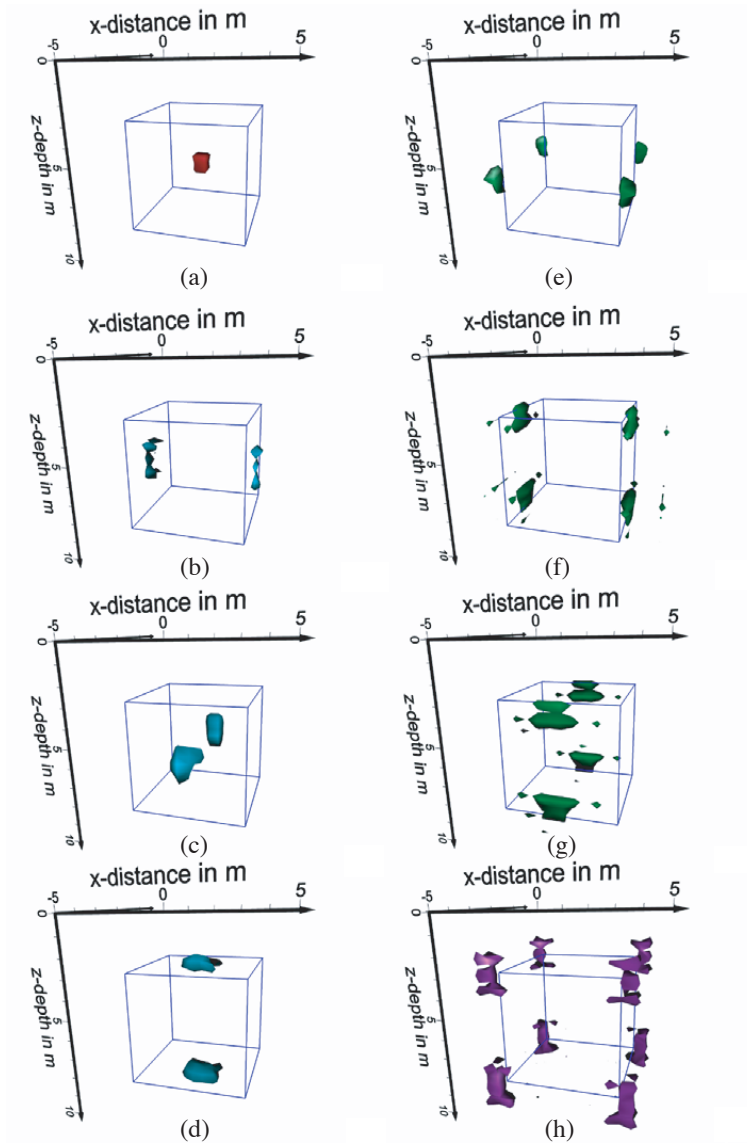
Figure 4. The SPOP (a), x-SDOP (b), y-SDOP (c), z-SDOP (d), xy-SQOP (e), xz-SQOP (f), yz-SQOP (g) and xyz-SOOP (h) tomographies derived from the SP synthetic map in Figure 3. The body with blue lines is the cube model.

(a)   (b)
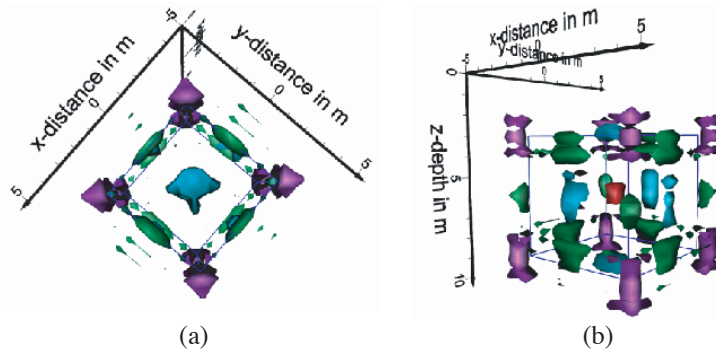
Figure 5. A joint representation of the SPOP (red), SDOP (light blue), SQOP (green) and SOOP (purple) nuclei, viewed from top (a) and laterally (b), useful to retrieve the source body of the SP map in Figure 3.

(x, y)-plane.

Figure 4 shows the results from the application of the multipole probability tomography algorithm to the SP map in Figure 3. Since no topographic effects have been simulated, the scanner functions used to compute the η-functions have been obtained from the previous formulae putting $z'_x = z'_y = 0$, $x'_\varphi = y'_\psi = 1$ and $g(z) = 1$. For the sake of clarity, in all of the 3D probability tomography plots we will show sufficiently small SPOP, SDOP, SQOP and SOOP nuclei, each enclosing the maximum absolute value (MAV) of the corresponding η-function.

The SPOP image shows a positive nucleus around the cube centre. The SDOP image shows, instead, three distinct doublets of nuclei with opposite signs very close to the centres of the corresponding opposite faces of the cube. Three distinct quadruplets appear around the centres of the cube sides in the SQOP tomographies of the off-diagonal terms, and an octoplet located at the vertices of the cube is the peculiar result from the SOOP image. The parameters of the nuclei in Figure 4 are listed in Table 1. A shift of 0.1 m along z-axis is estimated for the cube centre from its true position. Furthermore, an average error of about 3% affects the estimate of the side length of the cube, from the distance between the MAV points of two opposite nuclei in each multiplet.

The practical interest is to retrieve shape and position of the source body. Figure 5 suggests that a quick modelling can be done, by plotting into a single image all of the nuclei drawn in Figure 4.

Table 1. Characterization of the SPOP, SDOP, SQOP and SOOP nuclei in Figure 4. **A**: nucleus type; **B**: selected bounding isosurface level; **C**: maximum absolute value (MAV); **D**: (x, y, z) of the MAV point.

| A	B	C	D
SPOP (+)	$\eta_m^{(p)} = 0.950$	$\left\|\eta_m^{(p)}\right\|_{max} = 0.952$	(0.0, 0.0, 5.9)
x-SDOP (+)	$\eta_{n,x}^{(d)} = 0.450$	$\left\|\eta_{n,x}^{(d)}\right\|_{max} = 0.491$	(−3.1, 0.1, 6.0)
x-SDOP (−)	$\eta_{n,x}^{(d)} = -0.440$	$\left\|\eta_{n,x}^{(d)}\right\|_{max} = 0.467$	(3.1, 0.0, 6.0)
y-SDOP (+)	$\eta_{n,y}^{(d)} = 0.460$	$\left\|\eta_{n,y}^{(d)}\right\|_{max} = 0.494$	(−0.1, −3.0, 6.0)
y-SDOP (−)	$\eta_{n,y}^{(d)} = -0.440$	$\left\|\eta_{n,y}^{(d)}\right\|_{max} = 0.467$	(−0.1, 3.0, 6.0)
z-SDOP (+)	$\eta_{n,z}^{(d)} = 0.450$	$\left\|\eta_{n,z}^{(d)}\right\|_{max} = 0.481$	(0.0, 0.1, 3.0)
z-SDOP (−)	$\eta_{n,z}^{(d)} = -0.450$	$\left\|\eta_{n,z}^{(d)}\right\|_{max} = 0.484$	(0.0, 0.0, 9.0)
xy-SQOP (+)	$\eta_{g,xy}^{(q)} = 0.280$	$\left\|\eta_{g,xy}^{(q)}\right\|_{max} = 0.297$	(3.0, 3.0, 5.9) (−3.0, −3.0, 5.9)
xy-SQOP (−)	$\eta_{g,xy}^{(q)} = -0.280$	$\left\|\eta_{g,xy}^{(q)}\right\|_{max} = 0.297$	(3.1, −3.0, 6.0) (−3.0, 3.0, 6.0)
xz-SQOP (+)	$\eta_{g,xz}^{(q)} = 0.240$	$\left\|\eta_{g,xz}^{(q)}\right\|_{max} = 0.289$	(−3.3, 0.0, 3.1) (3.3, 0.0, 9.0)
xz-SQOP (−)	$\eta_{g,xz}^{(q)} = -0.240$	$\left\|\eta_{g,xz}^{(q)}\right\|_{max} = 0.284$	(3.3, 0.0, 3.1) (−3.3, 0.0, 9.0)
yz-SQOP (+)	$\eta_{g,yz}^{(q)} = 0.240$	$\left\|\eta_{g,yz}^{(q)}\right\|_{max} = 0.289$	(0.0, −3.2, 3.1) (0.0, 3.3, 9.0)
yz-SQOP (−)	$\eta_{g,yz}^{(q)} = -0.240$	$\left\|\eta_{g,yz}^{(q)}\right\|_{max} = 0.284$	(0.0, 3.2, 3.1) (0.0, −3.2, 9.0)
xyz-SOOP (+)	$\eta_{h,xyz}^{(o)} = 0.122$	$\left\|\eta_{h,xyz}^{(o)}\right\|_{max} = 0.129$	(3.1, 3.1, 3.0) (−3.1, −3.1, 3.0) (3.1, −3.1, 9.0) (−3.1, 3.1, 9.0)
xyz-SOOP (−)	$\eta_{h,xyz}^{(o)} = -0.122$	$\left\|\eta_{h,xyz}^{(o)}\right\|_{max} = 0.129$	(3.1, −3.1, 3.1) (−3.1, 3.1, 3.1) (−3.1, −3.1, 9.1) (3.1, 3.1, 9.0)

4.2. The Single Point Charge Model

The SP map in Figure 3 has a very close resemblance with the map due to a point charge. To this aim, we consider a point charge of $0.5\,\mathrm{C}$ placed at $x = 0$, $y = 0$, $z = 6\,\mathrm{m}$. The SP map has been computed at the nodes of a square grid with the same characteristics as in the previous case. Figure 6 depicts the SP map thus obtained.

Figure 7 shows the results from the application of the multipole tomography imaging. As in the coaxial cube case, the SPOP image gives a clear indication as to the correct position of the point charge. However, in spite of the fact that the source is a single pole, SDOP, SQOP and SOOP nuclei also appear so regularly located that, considered singularly, no difference can be detected with respect to the previous cube model. The situation changes considerably if we plot the SDOP, SQOP and SOOP nuclei altogether into a multipole image as in Figure 8. It is no longer possible, now, to combine a set of SDOP, SQOP and SOOP nuclei crossed by a single plane as in the previous case. In other words, a cube's face can no longer be traced. The multipole analysis seems thus able to differentiate the response of a cube from that of a point source.
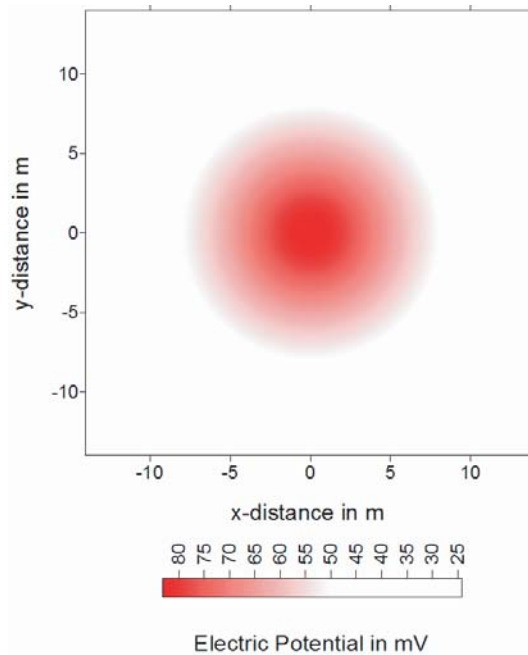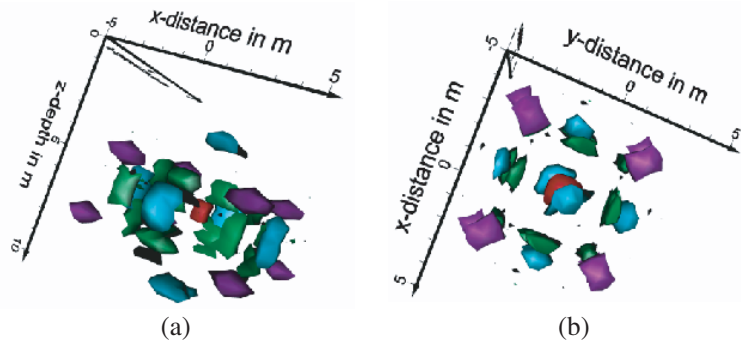

Figure 6. The SP map due to a point charge of $0.5\,\mathrm{C}$ placed at $x = 0$, $y = 0$ and $z = 6\,\mathrm{m}$.
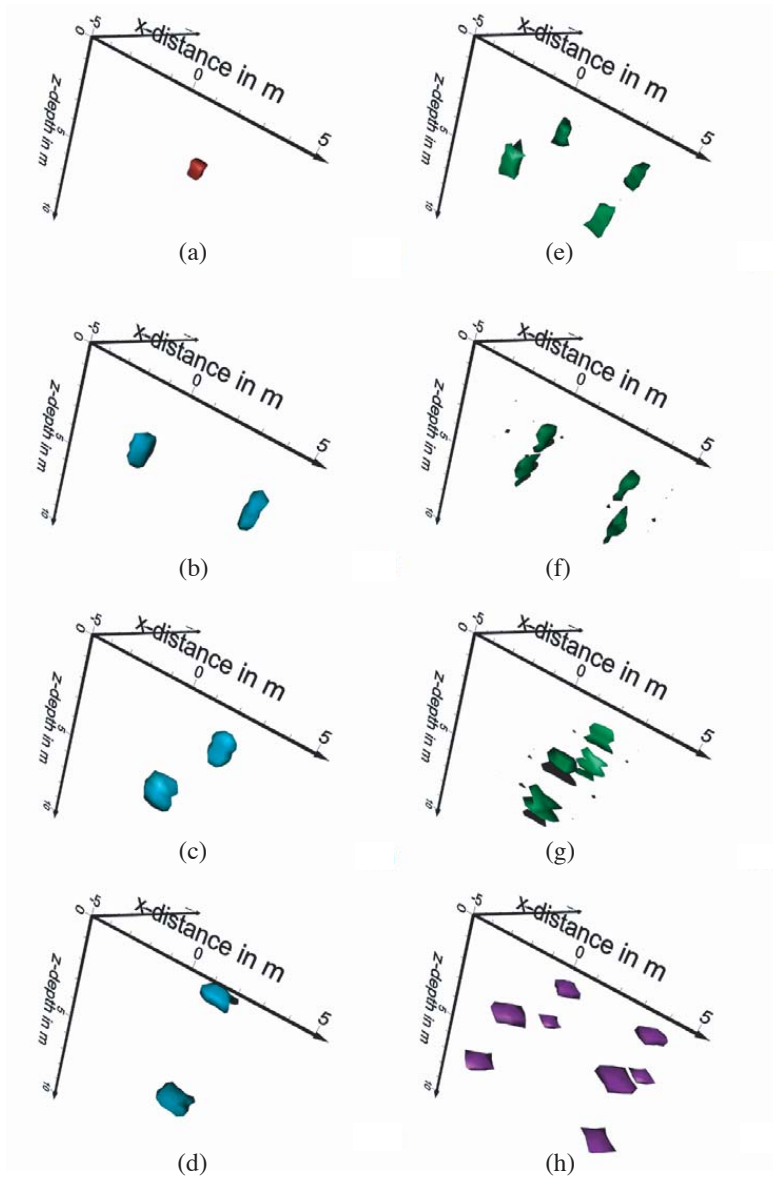
Figure 7. The SPOP (a), x-SDOP (b), y-SDOP (c), z-SDOP (d), xy-SQOP (e), xz-SQOP (f), yz-SQOP (g) and xyz-SOOP (h) tomographies derived from the SP map in Figure 6.

(a)   (b)

Figure 8. A joint representation of the SPOP (red), SDOP (light blue), SQOP (green) and SOOP (purple) nuclei under two different angles of view, derived from the SP map in Figure 6.

The fact that SDOP, SQOP and SOOP nuclei are developed also for the single point charge model must be interpreted as the consequence of the probability meaning attributed to the η-functions. These functions allow the points where they obtain the maximum occurrence probability to be detected. An array of multipoles is thus highlighted, providing a SP response equivalent to that of a single point source. In other words, the multipole source geometry in Figure 8 is likely to represent the most probable polyhedral figure generating a SP response equivalent to that drawn in Figure 6. The parameters of the SPOP, SDOP, SQOP and SOOP nuclei are listed in Table 2.

4.3. The Rotated and Tilted Cube Model

We show now what happens when the sides of the cube are no longer parallel to the reference coordinate axes. A new model is thus analysed by rotating the cube previously dealt with by 45° around both the vertical z-axis and y-axis through the centre. Figure 9 shows the SP map of this new source body configuration.

Figure 10 illustrates the results from the application of the multipole tomography imaging. The SPOP image still shows a nucleus located around the centre. On the contrary, the SDOP, SQOP and SOOP nuclei exhibit a mixed behaviour compared with that of the coaxial cube model. While in the former case they distinctly represent the faces, corners and vertices of the cube, respectively, now the same multiplets can simulate any of these geometrical features, depending on how the body is collocated with respect to the assumed reference coordinate system. Nevertheless, the nuclei are always revealed in

Table 2. Characterization of the SPOP, SDOP, SQOP and SOOP nuclei in Figure 7. **A**: nucleus type; **B**: selected bounding isosurface level; **C**: maximum absolute value (MAV); **D**: (x, y, z) of the MAV point.

| A	B	C	D
SPOP (+)	$\eta_m^{(p)} = 0.931$	$\left\|\eta_m^{(p)}\right\|_{max} = 0.933$	(0.0, 0.0, 6.0)
x-SDOP (+)	$\eta_{n,x}^{(d)} = 0.437$	$\left\|\eta_{n,x}^{(d)}\right\|_{max} = 0.453$	(−3.0, 0.0, 6.0)
x-SDOP (−)	$\eta_{n,x}^{(d)} = -0.437$	$\left\|\eta_{n,x}^{(d)}\right\|_{max} = 0.448$	(3.1, 0.0, 6.0)
y-SDOP (+)	$\eta_{n,y}^{(d)} = 0.440$	$\left\|\eta_{n,y}^{(d)}\right\|_{max} = 0.463$	(−0.1, −3.0, 6.0)
y-SDOP (−)	$\eta_{n,y}^{(d)} = -0.440$	$\left\|\eta_{n,y}^{(d)}\right\|_{max} = 0.448$	(0.0, 3.0, 6.1)
z-SDOP (+)	$\eta_{n,z}^{(d)} = 0.445$	$\left\|\eta_{n,z}^{(d)}\right\|_{max} = 0.462$	(0.1, 0.1, 3.1)
z-SDOP (−)	$\eta_{n,z}^{(d)} = -0.445$	$\left\|\eta_{n,z}^{(d)}\right\|_{max} = 0.464$	(0.1, 0.1, 9.1)
xy-SQOP (+)	$\eta_{g,xy}^{(q)} = 0.283$	$\left\|\eta_{g,xy}^{(q)}\right\|_{max} = 0.300$	(2.2, 2.2, 5.9) (−2.2, −2.3, 5.9)
xy-SQOP (−)	$\eta_{g,xy}^{(q)} = -0.283$	$\left\|\eta_{g,xy}^{(q)}\right\|_{max} = 0.300$	(2.2, −2.3, 5.9) (−2.2, 2.2, 5.9)
xz-SQOP (+)	$\eta_{g,xz}^{(q)} = 0.150$	$\left\|\eta_{g,xz}^{(q)}\right\|_{max} = 0.177$	(−2.5, −0.2, 4.5) (2.5, −0.1, 7.5)
xz-SQOP (−)	$\eta_{g,xz}^{(q)} = -0.150$	$\left\|\eta_{g,xz}^{(q)}\right\|_{max} = 0.177$	(2.5, −0.2, 4.5) (−2.5, −0.1, 7.5)
yz-SQOP (+)	$\eta_{g,yz}^{(q)} = 0.160$	$\left\|\eta_{g,yz}^{(q)}\right\|_{max} = 0.177$	(−0.2, −2.5, 4.6) (−0.1, 2.5, 7.5)
yz-SQOP (−)	$\eta_{g,yz}^{(q)} = -0.160$	$\left\|\eta_{g,yz}^{(q)}\right\|_{max} = 0.177$	(−0.2, 2.5, 4.5) (−0.1, −2.5, 7.5)
xyz-SOOP (+)	$\eta_{h,xyz}^{(o)} = 0.085$	$\left\|\eta_{h,xyz}^{(o)}\right\|_{max} = 0.100$	(2.0, 2.1, 4.5) (−2.0, −2.1, 4.4) (1.9, −2.1, 7.6) (−2.0, 2.1, 7.5)
xyz-SOOP (−)	$\eta_{h,xyz}^{(o)} = -0.085$	$\left\|\eta_{h,xyz}^{(o)}\right\|_{max} = 0.100$	(2.1, −2.0, 4.4) (−2.0, 2.0, 4.4) (−2.0, −2.0, 7.5) (2.0, 2.0, 7.5)
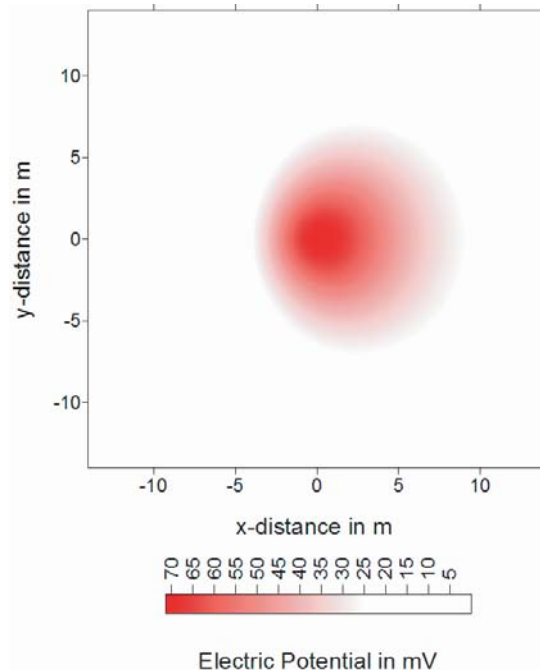
Figure 9. The SP map for the tilted cube model with same parameters as in Figure 3, rotated by 45° around the vertical and horizontal axes through the centre.

homologous pairs. However, it must be stressed that this behaviour is not casual, since the procedure simply implies the search for the MAV points of the first, second and third order crossed derivatives of the kernel function with respect to the reference axes. When plotted altogether, the SDOP, SQOP and SOOP nuclei still make possible to delineate the cubic shape of the source body, as clearly visible in Figure 11.

4.4. The Coaxial Two-prism Model

The forth example is the coaxial two-prism model, whose aim is to test the resolution power of the new tomography method. The first prism is a cube with $\Delta\sigma \cong 5.787 \cdot 10^{-4}\,\mathrm{C/m^2}$, and the second one is a parallelepiped with $\Delta\sigma = -4.822 \cdot 10^{-4}\,\mathrm{C/m^2}$. Three cases are shown with three different distances between the centres of the two prisms. Position and side lengths of the two bodies are detailed in the caption of Figure 12. The SP datasets have been computed at the nodes of a
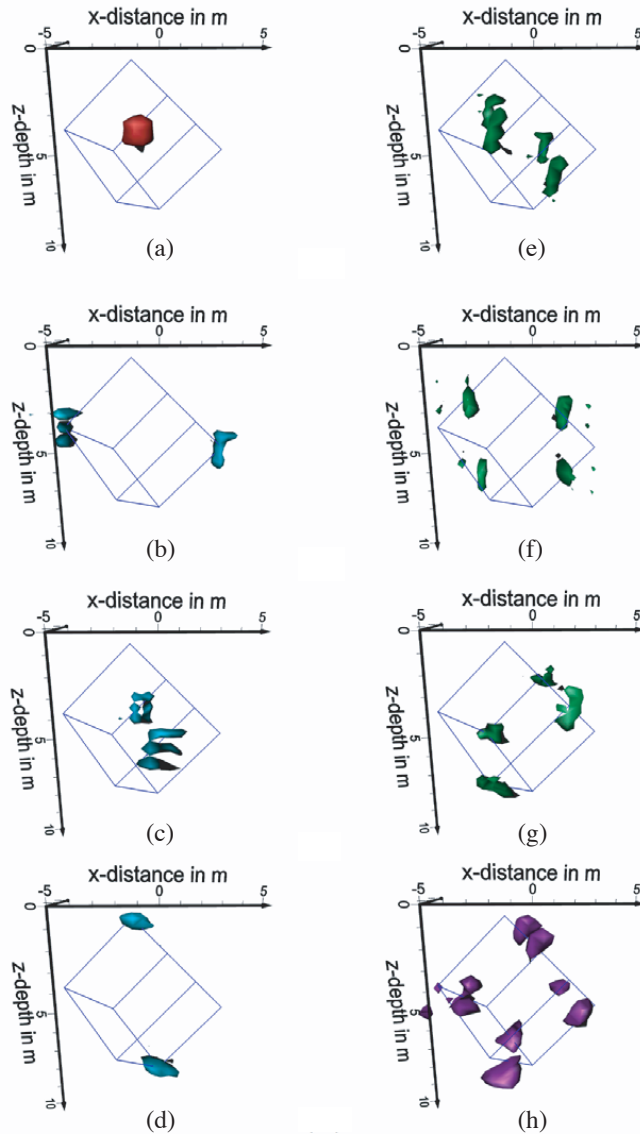
Figure 10. The SPOP (a), x-SDOP (b), y-SDOP (c), z-SDOP (d), xy-SQOP (e), xz-SQOP (f), yz-SQOP (g) and xyz-SOOP (h) tomographies derived from the SP synthetic map drawn in Figure 9. The body with light blue lines is the inclined cube model.

(a)   (b)
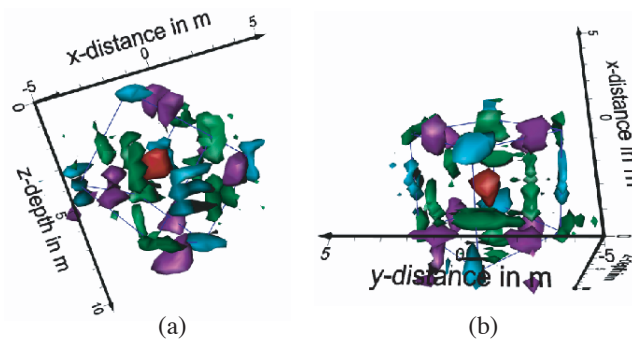
Figure 11. A joint representation of the SPOP (red), SDOP (light blue), SQOP (green) and SOOP (purple) nuclei, under two different angles of view, useful to retrieve the source body of the SP map in Figure 9.

square grid by a 1 m long step in the rectangle $[-60, 60] \times [-30, 30]\,\mathrm{m}^2$. Figure 12 shows the SP maps for the three cases in order of decreasing distance between the centres from the top (a) to the bottom plot (b). It is quite evident that the decreasing distance is the cause of an increasing compression of the SP contour lines in the region of highest mutual interference.

Figure 13 displays the tomography results for the three cases, where, for brevity, only the combined multipole images are reported. In the top one, which refers to a distance between the centres greater than 3 times the average side length of the bodies, the interaction between the two prisms is rather negligible and their true shape can still be recognised. In the middle image, which refers to a distance between the centres of about 2.5 times the average side length, all of the facing SDOP, SQOP and SOOP nuclei depart from their initial places to converge to the centre of the two bodies' system. Finally, in the bottom picture, which refers to a distance a little greater than 2 times the average side length, the detached facing nuclei of the same type are wholly melted midway between the prisms. The facing faces, corners and vertices of the two nearby bodies have therefore completely lacked resolution. This localised effect is not to be considered a weakness of the proposed multipole approach, but rather an intrinsic physical limitation due to the relatively small distance between the two bodies with respect to the depth of burial.

5. A FIELD CASE-HISTORY

As well documented, in natural hydrothermal systems SP signals are generated mainly by electrokinetic flows. Generally speaking, in active
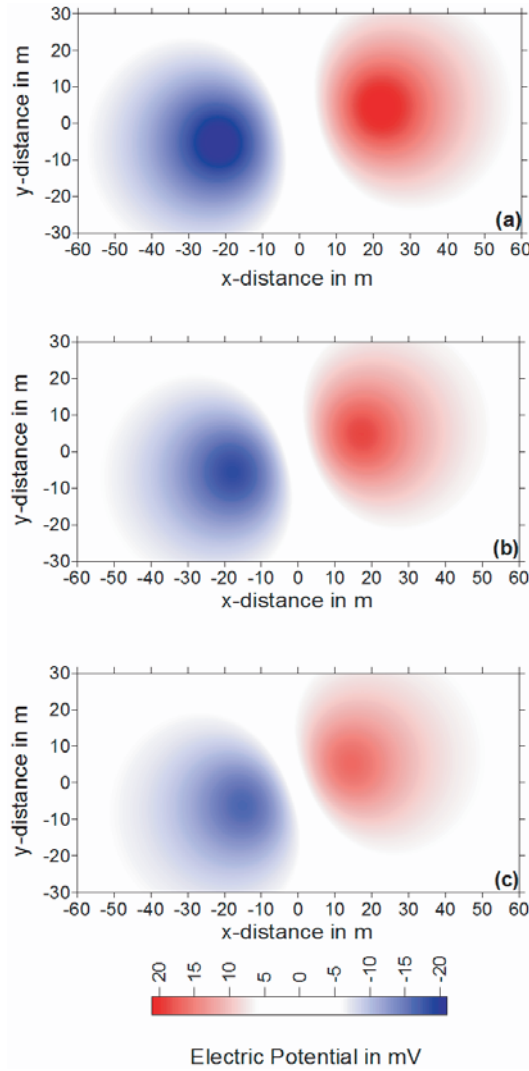
Figure 12. The SP map for the two-prism model made of: (1) a cube with $\Delta\sigma \cong 5.787 \cdot 10^{-4}$ C/m^2, sides parallel to the three coordinate axes and 12 m long each, and centre at $x = 20$ m (a), $x = 14.5$ m (b) and $x = 11$ m (c), $y = 4$ m, $z = 15$ m; (2) a parallelepiped with $\Delta\sigma \cong -4.822 \cdot 10^{-4}$ C/m^2, x- and z-oriented sides 13 m long and y-oriented sides 13.5 m long, and centre at $x = -20$ m (a), $x = -15$ m (b) and $x = -11.5$ m (c), $y = -4.75$ m, $z = 15$ m.

(a)

(b)   (c)
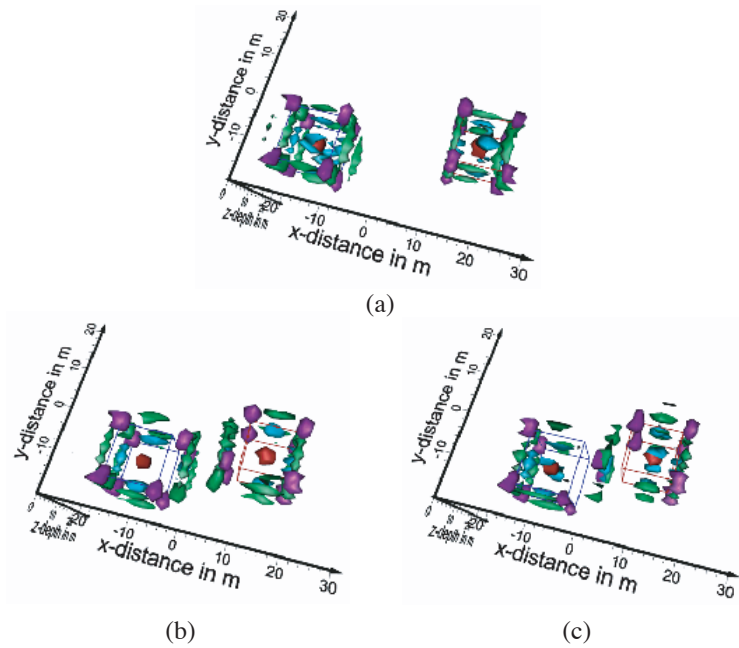
Figure 13. A joint representation of the SPOP (red), SDOP (light blue), SQOP (green) and SOOP (purple) nuclei for the two-prism model with decreasing distance between the centres of the two prisms. The sequence of the images is the same as that of the SP maps in Figure 12.

volcanic areas, SP positive anomalies correspond to upward migrating fluids, while negative ones to a downward fluid movement [9, 14].

We illustrate now the application of the SP 3D multipole probability tomography to an SP survey carried in the volcanic area of Mt. Somma-Vesuvius (Naples, Italy), which aimed to configure the main plumbing system of the volcanic complex. Mt. Somma-Vesuvius is a polygenic strato-volcano, whose most recent period of history (1631–1944) was characterized by a semipersistent, relatively mild activity (lava fountains, gases and vapour emission from the crater), frequently interrupted by short quiet periods that never exceeded seven years. From 1944 to the present time, Mt. Somma-Vesuvius has remained quiet.

The SP data were collected in 1996 by the gradient technique with a 100 m long passive dipole, continuously displaced along a wide net of randomly distributed circuits within an area of about $144 \, km^2$ [15],
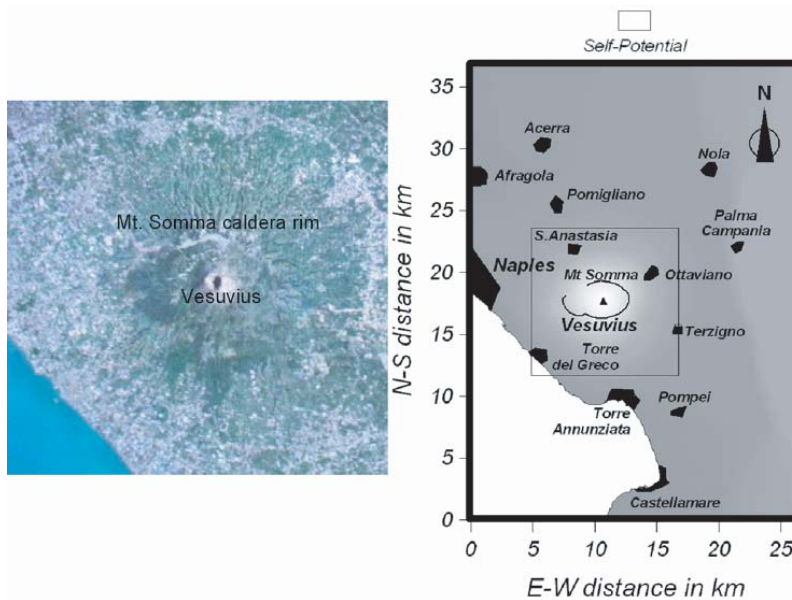
Figure 14. The Mt. Somma-Vesuvius survey area.

sketched in Figure 14. Figure 15 shows the behaviour of the SP field in mV, resulting from the processing of 1250 measurements [15, 16]. As the area is characterized by a strongly uneven topography, the 3D multipole tomography algorithm with topographic effects has been used. A similar SP map realised in 1995 was elaborated by the probability tomography method, limitedly, however, only to the source pole and dipole analysis [9, 15, 16].

The SPOP image in Figure 16 displays a pair of nuclei of opposite sign containing two poles with the highest occurrence probability. They are interpreted as the centres of the polarised bodies responsible of the SP biggest anomalies of opposite sign drawn in Figure 15. The negative and positive poles appear located, respectively, beneath the Somma caldera northern rim and the Vesuvius cone. Combining in pairs and altogether the SPOP, SDOP, SQOP and SOOP nuclei into single plots, the images in Figure 17 are obtained.

Figure 17 shows a quite regular assemblage of the SDOP, SQOP and SOOP multiplets. All the related nuclei appear clustered around the two poles of Figure 15, thus defining two distinct blocks. Compared with the results from the two-prism model, the two blocks appear so sufficiently distant from each other as to exclude any interaction between them, as in Example (a) in Figure 13. The parameters of

Table 3. Coordinates in km of the points with relative maximum absolute values for the SPOP, SDOP, SQOP and SOOP nuclei in Figure 17.

| Anomaly	SPOP (+)	SPOP (−)
SPOP	(5.4, 6.3, 1.5)	(6.5, 9.9, 0.9)
x-SDOP (+)	(4.3, 6.2, 1.6)	(7.3, 10.0, 1.0)
x-SDOP (−)	(6.9, 6.2, 1.6)	(5.4, 9.8, 1.0)
y-SDOP (+)	(5.3, 5.4, 1.8)	(6.3, 11.6, 1.0)
y-SDOP (−)	(5.3, 7.0, 1.7)	(6.4, 9.0, 0.9)
z-SDOP (+)	(5.5, 6.3, 0.9)	(6.4, 9.9, 1.9)
z-SDOP (−)	(5.5, 6.3, 2.7)	(6.5, 9.9, 0.4)
xy-SQOP (+)	(4.6, 5.5, 1.8) (6.5, 6.9, 1.8)	(5.5, 9.0, 1.2) (7.1, 11.5, 1.3)
xy-SQOP (−)	(4.6, 6.9, 1.8) (6.6, 5.5, 1.8)	(5.5, 11.3, 1.2) (7.1, 9.0, 1.3)
xz-SQOP (+)	(4.5, 6.0, 0.9) (6.5, 6.1, 2.7)	(5.4, 9.7, 0.2) (7.4, 10.2, 2.1)
xz-SQOP (−)	(6.5, 6.0, 0.8) (4.6, 6.1, 2.7)	(7.2, 9.9, 0.2) (5.2, 10.2, 2.2)
yz-SQOP (+)	(5.4, 5.2, 0.7) (5.4, 7.2, 2.6)	(6.3, 9.0, 0.3) (6.2, 11.6, 2.1)
yz-SQOP (−)	(5.2, 7.1, 0.7) (5.4, 5.2, 2.6)	(6.3, 11.3, 0.2) (6.3, 9.1, 2.1)
xyz-SQOP (+)	(4.5, 6.8, 0.7) (6.3, 5.3, 0.7) (4.7, 5.6, 2.7) (6.4, 7.0, 2.7)	(5.4, 8.8, 0.3) (6.9, 11.0, 0.2) (5.5, 11.2, 1.9) (7.0, 9.3, 2.0)
xyz-SQOP (−)	(4.6, 5.3, 0.7) (6.3, 5.6, 0.7) (4.7, 7.1, 2.7) (6.4, 6.8, 2.7)	(5.4, 10.8, 0.1) (6.9, 8.8, 0.3) (5.5, 9.3, 2.0) (7.0, 11.5, 2.3)

the SPOP, SDOP, SQOP and SOOP nuclei in Figure 17 are listed in Table 3, from which the source bodies are estimated to be confined within the first 3 km of depth b.s.l.

The geometry of the SP source bodies is now much better delineated than in the former study limited to the SPOP and SDOP analysis [9]. In conclusion, the SP field in the Mt. Somma-Vesuvius volcanic area can be explained by the existence of a shallow geothermal system, made of a single dominant convective cell. The descending branch of this circuit, where cooled fluids, occasionally mixed with

meteoric water, percolate, should reasonably correspond with the negatively charged block beneath the Somma caldera northern rim. The ascending branch, where the fluids heated from below rise up, should instead correspond with the positively charged block beneath the Vesuvius cone, and likely form the reservoir feeding the active fumaroles located in the top central crater.
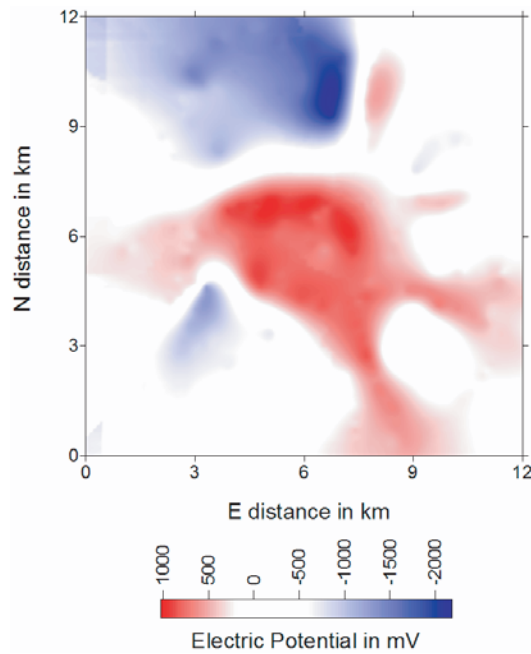
Figure 15. The Mt. Somma-Vesuvius SP map.
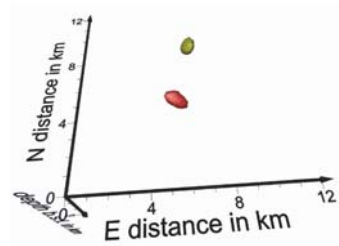
Figure 16. The Mt. Somma-Vesuvius 3D SPOP tomography of the SP map reported in Figure 15. The yellow and red nuclei represent the negative and positive poles, respectively.
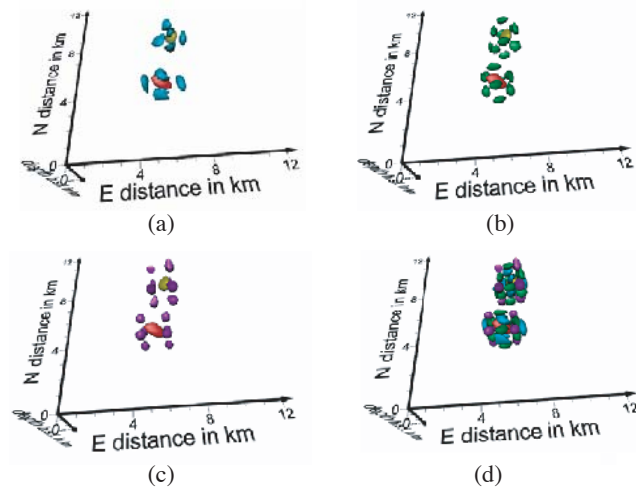
Figure 17. A joint representation of the SPOP and SDOP (a), SPOP and SQOP (b), SPOP and SOOP (c), SPOP, SDOP, SQOP and SOOP (d) nuclei, resulting from the application of the 3D multipole tomography method to the Mt. Somma-Vesuvius SP map in Figure 17.

6. CONCLUSION

We have exposed the theory of the 3D multipole probability tomography for the SP method by a generalised approach including a combination of poles, dipoles, quadrupoles and octopoles as elementary point sources of the SP anomalies. These physical sources have been used to detect the position of the centres of the true sources and to highlight the features of their boundaries. Improving the geometrical definition of the sources of the SP anomalies has thus been the main purpose of the new approach.

A few synthetic examples have been analysed in order to understand the full capabilities of the multipole probability tomography in the search for the most probable location and shape of the buried sources. Finally, a field case-history related to an SP survey carried out in the volcanic area of Vesuvius (Naples, Italy) has been presented in order to delineate the geometry of the SP sources in the central volcanic area within the first 3 km of depth below sea level.

To conclude, we emphasise the role of the tomography approach in the definition of the sources of the SP anomalies which are observed on the ground surface in many application fields, among which

volcanology, as in this study, seismology [17] and archaeology [10, 11]. We also stress the importance that the probability tomography can have in the study of the time evolution of the SP signals in high-risk volcanic areas, where the electrokinetic source field may undergo a rapid increase of intensity in conjunction with an increase of the volcanic emission activity. The 4D tomography is in fact becoming a very promising monitoring technique especially in fast flow visualization [18].

REFERENCES

1. Patella, D., "Introduction to ground surface self-potential tomography," *Geophys. Prosp.*, Vol. 45, 653–681, 1997.
2. Patella, D., "Self-potential global tomography including topographic effects," *Geophys. Prosp.*, Vol. 45, 843–863, 1997.
3. Mauriello, P. and D. Patella, "Resistivity anomaly imaging by probability tomography," *Geophys. Prosp.*, Vol. 47, 411–429, 1999.
4. Mauriello, P. and D. Patella, "Principles of probability tomography for natural-source electromagnetic induction fields," *Geophysics*, Vol. 64, 1403–1417, 1999.
5. Mauriello, P. and D. Patella, "Gravity probability tomography: A new tool for buried mass distribution imaging," *Geophys. Prosp.*, Vol. 49, 1–12, 2001.
6. Mauriello, P. and D. Patella, "Localization of maximum-depth gravity anomaly sources by a distribution of equivalent point masses," *Geophysics*, Vol. 66, 1431–1437, 2001.
7. Mauriello, P. and D. Patella, "Localization of magnetic sources underground by a probability tomography approach," *Progress In Electromagtics Research M*, Vol. 3, 27–56, 2008.
8. Mauriello, P. and D. Patella, "Resistivity tensor probability tomography," *Progress In Electromagtics Research B*, Vol. 8, 129–146, 2008.
9. Mauriello, P. and D. Patella, "Geoelectrical anomalies imaged by polar and dipolar probability tomography," *Progress In Electromagtics Research*, PIER 87, 63–88, 2008.
10. Alaia, R., D. Patella, and P. Mauriello, "Application of the geoelectrical 3D probability tomography in a test-site of the archaeological park of Pompei (Naples, Italy)," *J. Geophys. Eng.*, Vol. 5, 67–76, 2008.
11. Alaia, R., D. Patella, and P. Mauriello, "Imaging quadrupolar geophysical anomaly sources by 3D probability tomography. Ap-

plication to near surface geoelectrical surveys," *J. Geophys. Eng.*, Vol. 5, 359–370, 2008.

12. Landau, L. D. and E. M. Lifšits, *Elektrodinamika Splošnych Sred*, Nauka, Moscow, 1982.

13. Corwin, R. F., "The self-potential method for environmental and engineering applications," *Geotechnical and Environmental Geophysics*, S. H. Ward (ed.), Chap. 1: Review and Tutorial, SEG, 127–146, Tulsa, 1990.

14. Saracco, G., P. Labazuy, and F. Moreau, "Localization of selfpotential sources in volcano-electric effect with complex continuous wavelet transform and electrical tomography methods for an active volcano," *Geophys. Res. Lett.*, Vol. 31, 1–5, 2004.

15. Di Maio, R., P. Mauriello, D. Patella, Z. Petrillo, S. Piscitelli, and A. Siniscalchi, "Electric and electromagnetic outline of the Mount Somma-Vesuvius structural setting," *J. Volcanol. Geoth. Res.*, Vol. 82, 219–238, 1998.

16. Iuliano, T., P. Mauriello, and D. Patella, "Looking inside Mount Vesuvius by potential fields integrated geophysical tomographies," *J. Volcanol. Geoth. Res.*, Vol. 113, 363–378, 2002.

17. Lapenna, V., D. Patella, and S. Piscitelli, "Tomographic analysis of self-potential data in a seismic area of southern Italy," *Ann. Geofis.*, Vol. 43, 361–374, 2000.

18. Soleimani, M., C. N. Mitchell, R. Banasiak, R. Wajman, and A. Adler, "Four-dimensional electrical capacitance tomography imaging using experimental data," *Progress In Electromagtics Research*, PIER 90, 171–186, 2009.